Accurate Stress Intensity Factor Solutions for Unsymmetric Corner Cracks at a Hole

S.A. Fawaz
Air Force Research Laboratory
Wright-Patterson AFB, OH 45433
Tel: +1 (937) 255 6104, Fax: +1 (937) 656 4999
Scott.Fawaz@afrl.af.mil

Börje Andersson
Aeronautical Research Institute of Sweden
Box 110 21, SE-161 11 Bromma, Sweden
Tel: +46 (8) 555 490 00, Fax: +46 (8) 25 34 81
ba@ffa.se

Stress intensity factor, *K*, solutions for unsymmetric corner cracks at a hole subject to general loading were determined using a *hp*-version of the finite element method (FEM) in conjunction with a mathematical splitting scheme to enable efficient, accurate calculations. In traditional applications of the FEM, mesh generation is labor intensive; however, using the splitting scheme, stress intensity functions are obtained without explicitly including the crack in the FE mesh of the global structure. By using the *hp*-version of FEM, a set of K-solutions converging exponentially fast to the exact solution is obtained. The crack is analyzed in the local domain with easily generated FE meshes. All structurally significant crack shapes were considered; specifically, crack depth to crack length ratios (*a/c*) of 0.1 - 10.0, crack depth to sheet thickness ratios (*a/t*) of 0.10 - 0.99, and hole radius to sheet thickness ratios (*r/t*) = 0.2 - 10.0. The loading conditions were remote tension, remote bending, and pin loading (bearing). In addition, all combinations of *a/c*, *a/t* and *r/t* are analyzed at each side of the hole; thus more than 900 thousand solutions were developed with control of the error in the computed *K* solutions. Calculated relative error is generally much smaller than 1% along the entire crack front including the vertex regions. Laboratory test and in-service experience shows fatigue cracks at holes exhibit unsymmetric growth; thus, the need for the new solutions is paramount. Comparisons are made to solutions in the open literature. The new *K* solutions show the literature solutions are in general accurate for all three load conditions; however, for the extreme cases of *a/c*, *a/t*, and *r/t*; the literature solutions are in error as much as 50 percent. The new *K* solutions are to be implemented in AFGROW, the USAF crack growth analysis code available on the World Wide Web at http://fibec.flight.wpafb.af.mil/fibec/afgrow.html.

1 INTRODUCTION

Mechanically fastened joints, riveted or bolted, offer many options to the designer and have been used for centuries to join two or more structural members. For statically loaded structure, as a minimum a good joint design ensures the stress concentration at the fastener hole edge does not

exceed the yield strength of the material. This is also the case for cyclically loaded structure, however, now the designer must also satisfy fatigue requirements. The fatigue problem can be attacked in two ways; one, use stress levels below the fatigue limit of the material thus cracks never initiate; two, design the structure such that the slow crack growth life of the component is greater than its design service goal plus some factor of safety. For primary aircraft structure, excluding landing gear, the second approach is preferred and directed by civilian airworthiness authorities and military specifications. Assuming the simplest crack growth law, Paris law Eqn (1), the designer can meet the fatigue life requirements by choosing a material with good fatigue properties and designing to keep ΔK in an acceptable range.

$$\frac{da}{dN} = C\Delta K^n \tag{1}$$

da/dN	=	Crack growth rate
C,n	=	Material constants
ΔK	=	Stress intensity factor range

The focus of this research effort was to accurately calculate K to add fidelity to the fatigue life predictions of mechanically fastened joints. Specifically, K solutions were calculated for unsymmetric corner cracks at a centrally located hole in a finite width sheet subject to tension, bending, and bearing as shown in Figure 1. Numerous combinations of *a/c*, *a/t*, and *r/t* are analyzed at each side of the hole; specifically, crack depth to crack length ratios (*a/c*) of 0.1 - 10.0, crack depth to sheet thickness ratios (*a/t*) of 0.10 - 0.99, and hole radius to sheet thickness ratios (*r/t*) of 0.2 - 10.0. More than 907,500 solutions were developed with control of the error in all the computed K solutions. The relative error is generally much smaller than 1% along the entire crack fronts up to the vertices.

2 BACKGROUND

In-service[1], full-scale fatigue test[2], and laboratory component/coupon[3] fatigue test evidence indicates cracks in riveted joints commonly nucleate as corner cracks at the faying surface/rivet hole bore intersection. The exact solution for the stress intensity factor is not known. The pursuit of a numerical estimate for K began over twenty years ago with Smith and Kullgren[4] using the finite element alternating method and Heckmer and Bloom[5] as well as Raju and Newman[6] using the finite element method. An extensive summary of the numerical simulations to estimate K solutions for corner cracked holes has recently been compiled by Bakuckas.[7] The report documents K solutions calculated by various methods; conventional finite element method (FEM), finite element alternating method (FEAM), boundary element method (BEM), and three-dimensional weight function method (WFM). The K's are extracted from the analysis results using indirect or direct methods; the former derives K from energy, usually the energy release rate and the latter derives K directly from the forces (force method) or displacements (crack opening displacement, COD, method) solution. A more complete discussion on indirect and direct methods for calculating K can be found in references [8] and [9].

The *p*-version finite element code, STRIPE,[10] developed by the Aeronautical Research Institute of Sweden is used in the current investigation. Recall, in *p*-version FEA the number of elements is kept fixed and convergence is obtained by increasing the order of approximation of the shape functions, *p*, within each element; whereas, in the *h*-version convergence is obtained by increasing the number of elements. In STRIPE, a combination of the *h*- and *p*-version FEA is

used to obtain exponential convergence of the stress intensity factor solution by simultaneously decreasing the element size (increasing the total number of elements in the model) and increasing the *p*-level. At present, the maximum *p*-level available in STRIPE is 15. For a uniform order of approximation, the total number of degrees of freedom per element is[11]

$$DoF = \frac{(p+1)(p+2)(p+3)}{6} + 3(p+1) \tag{2}$$

DoF = Total degrees of freedom
p = Polynomial order of approximation

For cracks in bodies of finite dimension, usually the crack front intersects a geometric boundary. The point of intersection is called the *vertex*. The *K*-variation is very complicated near a vertex for crack fronts intersecting perpendicular to a stress free surface (as in our case). In fact, the gradient along the crack front in *K* is infinitely large at the vertex as described in section 3.2 and hence difficult to capture in a numerical analysis. This problem in our case is completely resolved by employing a strongly graded mesh not only in the neighborhood of the crack front, but also along the crack front towards the two vertices.

3 MODELING THEORY AND IMPLEMENTATION

3.1 *K*-EXTRACTION FROM FEA RESULTS

We briefly review our method for reliable extraction of stress intensity factors for general smooth edges in 3D domains. Consider a smooth edge, γ, in Figure 2. The angle, ω is assumed to be constant. In the present paper, we are interested in the special case when $\omega = 2\pi$ and γ has a part-elliptical shape. Denote by *r*, the distance (short) from the edge to a point, and θ ($-\omega/2 \le \theta \le \omega/2$) the polar angle. The displacements, **u** can be written in the form (excluding exceptional angles ω),

$$\mathbf{u}(r,\theta,x_3) = \sum_{\alpha=I,II,III} K_\alpha(x_3) r^{\lambda_\alpha} \boldsymbol{\Psi}_\alpha(\theta) + \text{smoother terms} \tag{3}$$

where $K_I(x_3)$, $K_{II}(x_3)$, and $K_{III}(x_3)$, are the mode I, mode II, and mode III stress intensity functions, where for example K_I is defined by,

$$K_I(x_3) = \lim_{r\to 0} \sqrt{2\pi} r^{(1-\lambda_I)} \sigma_2(r,0,x_3) \tag{4}$$

where $\sigma_2(r, \theta, x_3)$ is the normal stress in the local (1,2,3) system. The exponents λ_α (α = *I, II, or III* in the following) depend only on the local geometry and local boundary conditions (faces are traction free in our case). The functions $\boldsymbol{\Psi}_\alpha$ in Eqn. (3) are,

$$\boldsymbol{\Psi}_\alpha(\theta,\lambda_\alpha) = \begin{bmatrix} \Psi_{\alpha 1}(\theta,\lambda_\alpha) \\ \Psi_{\alpha 2}(\theta,\lambda_\alpha) \\ \Psi_{\alpha 3}(\theta,\lambda_{\alpha)} \end{bmatrix} \tag{5}$$

or

$$\boldsymbol{\Psi}_I(\theta,\lambda_I)=\beta_I\begin{bmatrix}(\kappa-Q_I(\lambda_I+1))\cos(\lambda_I\theta)-\lambda_I\cos((\lambda_I-2)\theta)\\0\\(\kappa+Q_I(\lambda_I+1))\sin(\lambda_I\theta)+\lambda_I\sin((\lambda_I-2)\theta)\end{bmatrix} \tag{6}$$

$$\boldsymbol{\Psi}_{II}(\theta,\lambda_{II})=\beta_{II}\begin{bmatrix}(\kappa-Q_{II}(\lambda_{II}+1))\sin(\lambda_{II}\theta)-\lambda_{II}\sin((\lambda_{II}-2)\theta)\\0\\-((\kappa+Q_{II}(\lambda_{II}+1))\cos(\lambda_{II}\theta)+\lambda_{II}\cos((\lambda_{II}-2)\theta)\end{bmatrix} \tag{7}$$

$$\boldsymbol{\Psi}_{III}(\theta,\lambda_{III})=\beta_{III}\begin{bmatrix}0\\\sin(\lambda_{III}\theta)\\0\end{bmatrix} \tag{8}$$

where $\kappa = 3\text{-}4\nu$, ν is Poisson's ratio, G the shear modulus, and

$$\begin{aligned}
Q_I &= -\left(\frac{\lambda_I-1}{\lambda_I+1}\right)\frac{\sin\left(\frac{\omega(\lambda_I-1)}{2}\right)}{\sin\left(\frac{\omega(\lambda_I+1)}{2}\right)}\\
Q_{II} &= -\frac{\sin\left(\frac{\omega(\lambda_{II}-1)}{2}\right)}{\sin\left(\frac{\omega(\lambda_{II}+1)}{2}\right)}\\
\beta_I &= \frac{2G}{\sqrt{2\pi}\lambda_I(\lambda_I+1)(1+Q_I)}\\
\beta_{II} &= -\frac{2G}{\sqrt{2\pi}\lambda_{II}((\lambda_{II}-1)+Q_{II}(\lambda_{II}+1))}\\
\beta_{III} &= \frac{4G}{\sqrt{2\pi}\lambda_{III}}
\end{aligned} \tag{9}$$

Table 1 shows λ_α-values for two technically important ω-values.

Table 1 Edge eigenvalues, λ_α

α	$\omega=3\pi/2$	$\omega=2\pi$
I	0.54448374	0.50000000
II	0.90852919	0.50000000
III	0.66666667	0.50000000

For smooth edges, the edge intensity functions $K_\alpha(x_3)$ are analytic on open intervals $s_k \le x_3 \le s_{k+1}$. Hence, we approximate the edge intensity functions K_α with the polynomials

$$\overline{K}_\alpha(x_3) = \sum_{n=0}^{p} \bar{k}_{\alpha n} P_n(s), \qquad s = \frac{2(x_3 - s_k)}{s_{k+1} - s_k} - 1 \tag{10}$$

where $\bar{k}_{\alpha n}$ are unknown coefficients, p is the polynomial order of the finite element trial functions, and P_n the Legendre polynomials.

Figure 3 illustrates a domain Ω^e used for extraction of the coefficients $\bar{k}_{\alpha n}$. The extraction domain has three cylindrical surfaces with circular cross sections ($\rho_2 > \rho_1 > \varepsilon$) perpendicular to the edge considered. We denote by Ω^e, the cylinder with inner radius ε and outer radius ρ_2. The surface of Ω^e is denoted Γ^e. The two outer cylindrical surfaces are exactly modeled in the finite element analysis.

The coefficients $\bar{k}_{\alpha n}$, we calculate by applying the Maxwell-Betti reciprocity theorem, Eqn. (11), p+1 times for each value of α.

$$\int_{\Gamma^e} \left(u_i^{(e)} T_i^{(n)} - U_i^{(n)} t_i^{(e)} \right) d\Gamma = \int_{\Omega^e} \left(u_i^{(e)} X_i^{(n)} - U_i^{(n)} x_i^{(e)} \right) d\Omega - \int_{\Gamma^e - \Gamma^e} \left(u_i^{(e)} T_i^{(n)} - U_i^{(n)} t_i^{(e)} \right) d\Gamma \tag{11}$$

In Eqn. (11), $u_i^{(e)}, t_i^{(e)}, x_i^{(e)}$ are the displacements, tractions, and volume force density, respectively, for a loading system having identical edge stress intensity functions K_α as the original load system. The fields $U_i^{(n)}, T_i^{(n)}, X_i^{(n)}$, $0 \le n \le p$, are auxiliary solutions used to calculate the coefficients $\bar{k}_{\alpha n}$.

As auxiliary displacement solutions, we use

$$U_i^{(n)}(s) = f(r) r^{-\lambda_\alpha} \mathbf{\Psi}_{\alpha i}(\theta, -\lambda_\alpha) P_n(s) \tag{12}$$

with $\mathbf{\Psi}_\alpha$ from Eqn. (6) to (8) and $f(r)$ being the cut-off function

$$f(r) = \begin{cases} 1 - 3\left(\dfrac{r - \rho_1}{\rho_2 - \rho_1} \right)^2 + 2\left(\dfrac{r - \rho_1}{\rho_2 - \rho_1} \right)^3 & \text{for } r \le \rho_1 \\ 1 & \text{for } \rho_1 < r < \rho_2 \\ 0 & \text{for } r \ge \rho_2 \end{cases} \tag{13}$$

The set of functions $U_i^{(n)}(s)$, which have a strong singularity at the edge, have desirable orthogonality properties with respect to $u_i^{(e)}$ and u_i correspond to identical edge stress intensity functions K_α.

Substituting u_i from Eqn. (3) and $U_i^{(n)}$ from Eqn. (12) into the left hand side of Eqn. (11), and shrinking $\varepsilon \to 0$, the unknown coefficient $\bar{k}_{\alpha n}$ is obtained as

$$\bar{k}_n = C_n \left(\int_{\Omega^e} \left(u_i^{(e)} X_i^{(n)} - U_i^{(n)} x_i^{(e)} \right) d\Omega - \int_{\Gamma^e} \left(u_i^{(e)} T_i^{(n)} - U_i^{(n)} t_i^{(e)} \right) d\Gamma \right) \tag{14}$$

In Eqn. (14), C_n is a material dependent constant. Displacements obtained from the finite element solution are substituted for $u_i^{(e)}$ in Eqn. (14). The extraction functions $U_i^{(n)}$ and the corresponding tractions $T_i^{(n)}$ vanish on the outer surface (radius ρ_2) of the extraction domain Ω^e. (Figure 3) because of the cylindrical cross-section and the cut-off functions Eqn. (13) used. The accuracy of the calculated stress intensity factors thus will mainly depend on a weighted average of the finite element solution inside the extraction domain. This gives the very fast convergence, with increasing *p* to the exact solution.

3.2 SOLUTION BEHAVIOR CLOSE TO VERTICES

The stress intensity functions show a complex behavior near the two vertices where the crack fronts intersect with the traction free surfaces (Figure 7 - Figure 13). The solution behavior in these regions is important since the maximum values of the stress intensity functions are to be found there. The mathematical theory for the vertex behavior is known in general form. A few details are here given from the theory and we exemplify that our numerical results are very accurate along the entire crack front, i.e. also arbitrary close to the vertices, and, in agreement with the basic mathematical findings. An analytical expression, derived from the mathematical theory, describes the near-vertex behavior including the region of maximum stress intensity. The simplicity of this expression makes it possible to store accurate stress intensity factor distributions in very compact form.

In spherical coordinates (ρ,ω,φ), the Cartesian displacements (u,v,w) near a vertex, for a straight crack front, can be written,[12]

$$\begin{bmatrix} u(\rho,\omega,\varphi) \\ v(\rho,\omega,\varphi) \\ w(\rho,\omega,\varphi) \end{bmatrix} = \sum_{j=1}^{J} B^{(j)} \rho^{\Lambda_j} \begin{bmatrix} \Theta_1^{(j)}(\omega,\varphi) \\ \Theta_2^{(j)}(\omega,\varphi) \\ \Theta_3^{(j)}(\omega,\varphi) \end{bmatrix} + \text{higher order terms} \tag{15}$$

where the scalars $B^{(j)}$ are so-called vertex intensity factors. In case of curved crack fronts, the expansion (15) has to be augmented with higher order terms. However, in all the cases studied here the two leading terms in Eqn. (15) stay the same. The functions $\Theta_i^{(j)}$ have the standard square root singularity for angles (ω,φ) corresponding to points close to the crack front.[13] For simplicity, we discuss only the pure mode I case (bending and traction loading). For a Poisson's ratio of 0.3 and a quarter elliptical crack, we have the universal constants $\Lambda_1 = 0.54782$, $\Lambda_2 = 1.21826$ which were calculated using the STRIPE-code and a spherical mesh at the vertex. From the definition of the stress intensity factor $K_I = \lim_{r\to 0} \sqrt{2\pi r}\,\sigma(r)$, r being the distance to the crack front and σ the normal stress, we get, using Eqn. (15), that the stress intensity function near the vertex must satisfy,

$$\frac{K_I(s)}{\sqrt{\frac{\pi a}{Q}}} = S_1(s/a)^{\Lambda_1 - 1/2} + S_2(s/a)^{\Lambda_2 - 1/2} + \text{higher order terms} \qquad (16)$$

where s is a coordinate along the crack front. S_1 and S_2 depends on (*a/c, a/t, r/t*) and the type of loading. The stress intensity functions K_I are always zero at the vertex (s=0) since $\Lambda_1 > 1/2$. The very steep gradient in K_I close to a vertex is in our case due to the fact that $\Lambda_1 \approx 1/2$. The parameters S_1 and S_2 can be determined from a fit to calculated numerical data close to the vertex. We see from Eqn. (16) that for small s, $K_I(s)/s^{\Lambda_1 - 1/2}$ is a linear function of $s^{\Lambda_2 - \Lambda_1}$. The analytical expression, Eqn. (16) can be used to accurately calculate K_I arbitrary close to the vertex, or the maximum value of K_I near the vertex. The point s^* where the stress intensity function is maximum is, for $S_2 < 0$ obtained from Eqn. (16), neglecting higher order terms, as,

$$s^* = a\left(\frac{S_1(\Lambda_1 - 1/2)}{S_2(\Lambda_2 - 1/2)}\right)^{\frac{1}{\Lambda_2 - \Lambda_1}} \qquad (17)$$

The corresponding stress intensity factor K_I is obtained after inserting $s = s^*$ into Eqn. (16). The two scalars S_1 and S_2, together with Eqns. (16) and (17) and the universal constants Λ_j, carry much information and are stored for each of the crack configurations analyzed.

3.3 SPLITTING SCHEME

A mathematical *splitting method* was used to efficiently and reliably calculate the 907,500 stress intensity factor solutions for unsymmetric part-elliptical cracks growing from a hole. A brief overview is given here; however, for a complete discussion of the mathematical theory, see references [14-16]. In the splitting method, the 3D fracture mechanics problem is split into three sub-problems, a complex multi-site cracking scenario is shown in Figure 4 although the current investigation is only considering two cracks at one hole, with the solution obtained by superposition of the sub-problems.

a. Global Crack Free Problem: The solution of the global crack free problem, see Figure 5, is $U_G^{(0)}$ and the only result required from the finite element analysis is the stress distributions on the surfaces where the cracks are to be located. Thus, this sub-problem is independent of the number and size of cracks under consideration.

b. A Set of M Local Problems: A local model is developed for each *a/c* and *c/r* to be analyzed (in our case, 275 local models where used to derive the 907,500 solutions). The applied load consists of L different normalized crack surface tractions with the solutions denoted as $\left\{U_L^{(m,l)} \middle| m = 1, 2 \ldots M, l = 1, 2, \ldots L\right\}$. The local models contain a single crack. By making the local models large in the thickness direction, only one FE-analysis is needed independently of the *a/t* ratio of interest. Figure 6 shows a very small part of a local mesh, designed for our *hp*-version of the FE method, for parameters *a/c* = 0.8, *c/r* = 0.125. Close to the crack front another five

cylindrical layers of elements are introduced which are not visible in the figure. So-called blended mapping is used in the analysis to describe the exact shape of the crack and the cylindrical hole surface. The results required from the local models are the tractions and displacements on an arbitrarily selected surface, Γ_i (dashed line in Figure 4) which encloses the entire crack in addition to the stress intensity functions $K_I(s)$, $K_{II}(s)$, and $K_{III}(s)$ for all the crack face loadings.

c. A Set of Global Crack Free Problems: The global model in a. is analyzed with prescribed *jumps* in the tractions and displacements at the surfaces Γ_i used in the local problems. Thus, the output from the local problems is input to the load calculations in the global models. The solutions are denoted as $\left\{U_G^{(m,l)} \middle| m = 1, 2 \ldots M, l = 1, 2, \ldots L\right\}$.

Solution of complex, 3D fracture mechanics problems are obtained by proper superposition of sub-problems a-c. The approximate displacement solution, $\overline{U}$ to the exact 3D solution, U is written as[17]

$$\overline{U} = U_G^{(0)} + \sum_{m=1}^{M}\sum_{l=1}^{L} \alpha_{(m,l)} U_G^{(m,l)} - \sum_{m=1}^{M}\sum_{l=1}^{L} \alpha_{(m,l)} U_L^{(m,l)} \tag{18}$$

where $\alpha_{(m,l)}$ are scaling factors determined by solving a small set of linear equations. Thus, with the known $U_G^{(0)}, U_G^{(m,l)}$, and $U_L^{(m,l)}$, the solution, $\overline{U}$ can be calculated with virtually no computational cost/crack configuration. This made it possible to derive almost one million basically error free *K*-solutions for the three loading cases. The computational efficiency of the strategy devised makes it feasible to use the calculated stress intensity data in Monte Carlo type studies of 3D multiple-site fatigue crack growth.[17] If global geometric non-linearity is significant for the structure being analyzed, sub-problem a. is solved as a fully three-dimensional non-linear problem.

4 RESULTS AND DISCUSSION

As discussed above, two finite element models, global and local, with $\nu = 0.3$ are used to calculate the stress intensity functions for each crack geometry. The global model, shown in Figure 5, is quite large with $2b = 2h = 200r = 400$ units where b and h are the half width and height, respectively. The hole radius is 2.0 units; thus, $r/b = r/h = 0.01$ resulting in negligible finite width/height effects for all crack lengths considered. The thickness, t, can easily be scaled to obtain K solutions for various r/t ratios. Blended function mapping is used to ensure the hole has an exact cylindrical surface and the crack front has an exact elliptical shape, see Figure 6.[18] In the z-direction, thickness direction, four layers of elements are used with relative thickness of 1, 7, 49, and 343 units, respectively. The mesh is designed for the *hp*-version of the finite element method; thus, seven elements are used along the crack front with relative lengths of 1, 7, 49, 343, 49, 7, and 1 unit. By using this highly graded mesh, the strong variation of the stress intensity function close to the crack vertices are captured with high accuracy. The K variation along the crack front is given in the form of piecewise polynomials as described in section 3.1. Close to the vertices, an analytical expression based on the mathematical expansion, Eqn. (16),

of K close to the vertex is used (section 3.2). Incidentally, the highly graded mesh was designed to accurately calculate K's for cracks that have nearly penetrated the back free surface, $a/t = 0.95$ and 0.99; however, this same mesh design also yields K solutions of the same accuracy for very shallow cracks, $a/c < 0.2$. These low aspect ratio solutions will be most useful in fatigue life prediction for bending dominant problems and corrosion/fatigue where shallow surface corrosion damage can begin to propagate in the cycle domain although damage initiated in the time domain.

The global model has 576 elements resulting in over 70,000 *DoF* at $p = 6$. The global mesh is overly refined for all of the crack shapes considered except when $a/t = 0.95$ and 0.99 where careful mesh refinement in the ligament between the crack depth and free surface is required. The local models contains approximately 1000 elements giving 140,000 *DoF* at $p = 6$. Exponential convergence of the finite element solution is possible when using the *hp*-version as seen in Figure 7 where convergence is obtained already at $p = 3$ for $2\phi/\pi \le 0.9$. Higher p-levels are required for $2\phi/\pi > 0.9$ due to the finite thickness effect[19] and large stress gradient at the hole edge. For more extreme crack geometries, the most extreme case being shown in Figure 8, higher p-levels are required than for all the other solutions. In fact, the error for lower p-levels could be increased drastically by using more than $(p\text{-}1)^2$ terms in Eqn. (18). However, we have had no difficulties in obtaining very accurate solutions using the model presented in section 3 and solutions for polynomial order p=6. Although error is much larger for small p, the accuracy of the $p = 6$ solution is still less than 0.5% as are all the other solutions.

Stress intensity factor solutions derived in the past using FEA or FEAM have typically used a quarter plate model assuming two symmetry planes, yz-plane at x = 0 and xz-plane at y = 0 in Figure 5, to reduce the number of degrees of freedom in the model thereby reducing the solution time. In this effort, no planes of symmetry are employed; thus, K's for each crack configuration, one or two cracks at the hole edge, are explicitly calculated without the need for the well-known Shah correction factor for converting K's for one crack to two cracks at a hole and vice versa.[20] The results of the Bakuckas round-robin are shown in Figure 9 where the solid lines indicate the upper and lower bounds of all solutions and ±3% deviation from the average solution. Two STRIPE analyses were conducted, one modelling the crack in an infinite plate (open squares) and the other using the same plate dimensions as that used by Bakuckas (open circles). Both of our analyses used a p-level of 6 to obtain the converged solution with error control. The 5% maximum difference between our solutions illustrate the well-known finite height/width effect. For this case we also made an independent check, by modelling half the domain explicitly, and solving the problem for $p = 2, 3, \ldots 10$, to verify convergence. Stress intensity functions were computed from the basic definition, $K_I = \lim_{r\to 0} \sqrt{2\pi r}\,\sigma(r)$ at a distance of $a/5000$ from the crack front. Our previous results were confirmed to the 3rd digits accuracy at all control points. Hence, we did not use the splitting method and the technique described for K-extraction described in section 3.1, but arrived at (practically) identical results. Therefore, we can guarantee that the STRIPE-solution shown in Figure 9 is the *exact* solution (with actual resolution) to the boundary value problem proposed by Bakuckas. Thus, of the six methods used and for the given crack configuration in the round-robin, the K's calculated using WFM and DIM where the most accurate, less than 2% error compared to the current results. In addition the FEM, FEAM, and BEM are 3% – 6% over conservative for this particular crack configuration. As will be discussed later, the error can be over 50% for some loading conditions and crack configurations.

Comparisons to the Newman/Raju solutions were also made for shallow and deep double cracks at a hole as shown in Figure 10 – Figure 12 for tension, bending, and pin loading. The Newman/Raju solutions were used as the reference solution; therefore the error is defined as

$$\text{Percent Error} = \frac{K_{Newman/Raju} - K_{STRIPE}}{K_{Newman/Raju}} \cdot 100 \tag{19}$$

Since K_I is zero at the vertex, we used our peak K_I in the vicinity of the vertex to compare to the Newman/Raju FEA results at $2\phi/\pi = 0$ (*c*-tip) and 1.0 (*a*-tip). The errors for each of the load cases at both the *c*-tip and *a*-tip are given in Table 1. For the *c*-tip, the errors are relatively small, although for $a/t = 0.8$, an underestimation of the bending *K* by 9% is alarming. Interestingly, large errors were found away from the vertices as well, see Figure 11A, where the error is approximately 30% in bending.

Table 2 Comparisons of Newman/Raju Solutions to STRIPE

	a/c = 0.2, r/t = 1.0					
	Tension		Bending		Pin Loading	
Location	a/t = 0.8	a/t =0.2	a/t = 0.8	a/t =0.2	a/t = 0.8	a/t =0.2
c-tip	3%	3%	-9%	1%	2%	-0.12%
a-tip	-20%	-47%	-10%	-48%	-24%	-55%

The error at the vertices, the location where the crack front intersects the free surface, is in general larger for the *a*-tip than *c*-tip. Figure 9 clearly shows *K* goes to zero at both vertices for Mode I loading. Interestingly, for wedge loading, Mode II and III *K*'s go to infinity. The *a*-tip vertex behavior dictates when the crack will penetrate the thickness of the plate. Currently, NASGRO[21] and AFRGOW[22] both use empirically based criteria to determine break-through. Using accurate *K* solutions at this location, as presented in Figure 10 - Figure 12, is the first step in removing the empiricism from this important crack growth behavior. Not only is the vertex behavior underestimated in Figure 10 - Figure 12, but also exhibits the wrong trend for the crack geometry shown in Figure 13. For this case, the Newman/Raju results overestimate $K_I(c)$ and underestimate $K_I(a)$. For all the crack geometries presented here, the Newman/Raju $K_I(a)$ is not accurately calculated; thus, accurate crack shape development is unlikely. Using *h*-version FEA to calculate *K*'s for part-elliptical cracks is always problematic because including sufficient mesh refinement between the *a*-tip and the near free surface is difficult. This appears to be the case for the Newman/Raju solutions.

In reference [23], Newman/Raju fit the finite element results presented in [6]. In NASGRO, the equations from [23] have been implemented. In NASGRO, three fitting parameters have been added to the original Newman/Raju[6] solutions; however, these three parameters were not included here in order to make a direct comparison between numerical results. The most significant of the three fitting parameters is β_R,[24] which is an empirically based function of the stress ratio, R, and is used to account for the plane stress to plane strain transition where the crack front intersects a free surface. For $R = 0$, $\beta_R = 0.9$ which results in a 10% reduction in the percent error in Table 1.

The Newman/Raju solutions are given for parameter range $0.2 \le a/c \le 2.0$, $a/t < 1.0$ in tension, $a/t < 0.8$ in bending, $0.5 \le r/t \le 2.0$, and $(r+c)/b < 0.5$. The other solutions in [7] have similar limits of applicability. Extrapolating these results, Newman/Raju for example, can yield large errors in the stress intensity factor. For a crack with $a/c = 10.0$, $a/t = 0.99$, and $r/t = 1.0$; Newman/Raju overestimate $K_I(c)$ by 14% and underestimate $K_I(a)$ by 59% in pure tension, but underestimate $K_I(c)$ by 91% and overestimate $K_I(a)$ by 60% in pure bending. The intent here is not to comment on the quality of the Newman/Raju solutions since they were landmark

achievements at the time of development, but to illustrate the danger in extrapolating *K* solutions. Additional comparisons of crack geometries outside the limits of the Newman/Raju solutions indicate the bending solution is most sensitive to the degree at which the geometry is outside the limits.

The most widely used approximation used to convert *K* solutions derived for one crack at a hole to two cracks at a hole (diametrically opposed) and vice versa was derived by Shah nearly 25 years ago.[25] The functional form is simple as seen by Eqn. (20).

$$\frac{K_{1crack}}{K_{2cracks}} = \sqrt{\frac{\frac{4}{\pi}+\frac{1}{2}\left(\frac{a}{t}\right)\left(\frac{a}{c}\frac{r}{t}\right)^{-1}}{\frac{4}{\pi}+\left(\frac{a}{t}\right)\left(\frac{a}{c}\frac{r}{t}\right)^{-1}}} \tag{20}$$

a/t = Crack depth/thickness
a/c = Crack length/crack depth
r/t = Hole radius/thickness

Using equations presented in [26], an additional correction factor was investigated here; however, as the crack length increases, the results diverge from Shah's. Eqn. (20) appears to be dependent on the crack shape, *a/c*, and crack size (area), *a/t*; however, Shah assumed the conversion factor was constant along the entire crack front. In addition, the Shah conversion factor is independent of applied load. Using the data from the current effort, these assumptions can be fully investigated considering all crack shapes and load cases, but has yet to be completed. A cursory examination of the validity of Eqn. (20) was conducted for very extreme crack configurations, $0.1 \le a/c \le 10.0$, $a/t = 0.99$, $r/t = 1.0$. For the given crack geometries, the maximum error in the Shah correction factor when compared to the current results at the *c*-tip for tension, bending, and bearing is 3%, 6%, and 9%, respectively, see Figure 14A. In practice, the Shah correction factor is applied at both the *c*- and *a*-tip; thus, errors in the correction factor not only affect the fatigue life prediction, but also the flaw shape development. The maximum error at the *a*-tip for tension, bending and bearing is 5%, 17%, and 7%, respectively, see Figure 14B. The $K_{1crack}/K_{2\ cracks}$ value from the STRIPE results did not vary significantly along the crack front for these "extreme" crack configurations. Additional comparisons are required to make a more general evaluation of the Shah correction factor.

To evaluate the effect of the second (unsymmetric) crack on the first crack, an influence factor, *M* is defined by Eqn. (21). *M* indicates the change in the *K* at crack 1 when the size (and shape) of crack 2 changes.

$$M(c_1,c_2) = \frac{K \text{ at } c_1 \text{ due to Unsymmetric Crack at } c_2 (c_1 \neq c_2)}{K \text{ at } c_1 \text{ due to Symmetric Crack at } c_2 (c_1 = c_2)} \tag{21}$$

Specifically, the *K* at crack 1 with an unequal size crack 2 (unsymmetric case) is normalized by the *K* at crack 1 with an equal size crack 2 (symmetric case). Two cracking scenarios, small and large, were considered for this investigation, both subject to pure remote tension. For the small

crack scenario, one crack size/shape ($a/c_1 = 0.2$, $a/t = 0.99$, $r/t = 1.0$) was held constant while the diametrically opposed crack size/shape ($0.2 \le a/c_2 \le 10.0$, $a/t = 0.2$, $r/t = 1.0$) varied. For the large crack scenario crack size/shapes were $a/c_1 = 0.1$, $a/t = 0.99$, $r/t = 1.0$ and $0.1 \le a/c_2 \le 10.0$, $a/t = 0.99$, $r/t = 1.0$, respectively. As illustrated by Figure 15, note the expanded scale on the ordinate, $K(c_1)$ for both the small and large cracks are weakly dependent on the size of the second crack, c_2. For example, at $c_2/c_1 = 0.01$, c_1 is 100 times larger than c_2; however, $K(c_1)$ for the small crack is less than 2% lower than the case where c_1 and c_2 are the same size (symmetric cracks, $c_2/c_1 = 1.0$). Similar behavior is seen for the large cracks where $K(c_1)$ is 12% lower than the case where $c_1=c_2$. Thus, the existence of the second crack is of more importance than the size. For these two cases, the $K(c_1)$ variation is also dependent on the crack shape (a/c) and crack area (a/t). As a result, any conversion factors to account for this behavior must be a function of both a/c and a/t.

The K values calculated near the a- and c-tip vertices were used along with Eqn. (16) to determine the parameters S_1 and S_2, which in turn are used along with Eqn. (17) to calculate the maximum K in the vicinity of each vertex. Figure 16 shows such a graph for the case for two symmetric corner cracks with $a/c = 0.8$, $a/t = 0.2$, $r/t = 2$ for the two vertices. We see that calculated stress intensity factors at all points, not at a vertex, falls almost perfectly on a straight line, as predicted by the mathematical theory, see also reference [27]. Note that the closest points are only $\approx a/2000$ from the vertices in this case. The conclusion is that stress intensity data obtained with our *hp*-version of FEM are accurate up to the two vertices. Lastly, the maximum $K_I/\sqrt{(\pi a/Q)}$ in the vicinity of the c-tip is 2.62 located 0.0.0059 units from the vertex and at the a-tip 3.24 and 0.0068, respectively. The corresponding parametric angle of the ellipse, ϕ for the maximum $K_I/\sqrt{(\pi a/Q)}$'s are 1.34° and 88.45°. All crack growth codes assume a value for ϕ based on engineering judgment or experimental evidence in an attempt to capture the maximum K at the a- and c-tips; however, as the present analysis shows, this dubious assumption is no longer required.

5 CONCLUSION

Highly accurate stress intensity factor solutions for diametrically opposed unsymmetric part-elliptical corner cracks at a hole subject to remote tension, remote bending, and bearing have been developed for all structurally significant crack configurations likely to occur in aircraft load bearing structure. The specific crack configurations investigated were $0.1 \le a/c \le 10.0$, $0.1 \le a/t \le 10.0$, and $0.2 \le r/t \le 10.0$. In total, 907,500 K solutions were generated and are currently being implemented in AFGROW. The accuracy, less than 0.5% for all crack cases considered, of the *hp*-version FEA as well as mathematical *splitting scheme* has been unequivocally proven and demonstrated. The location and magnitude of the maximum K at the a- and c-crack tips has been determined with less than 1% error. Any further work in this area should concentrate on improving the less than 1% error in the stress intensity factor shown here; although the authors do not know such a need.

6 REFERENCES

[1] Steadman, D., A. Carter, and R. Ramakrishnan. "Characterization of MSD in an In-Service Lap Joint." Proc. of The 3rd Joint FAA/DoD/NASA Conference on Aging Aircraft, September 20-23, 1999, Albuquerque, NM.

[2] Piascik, Robert S. and Scott A. Willard. The Growth of Multi-Site Damage in Fuselage Lap Joints. Proc. of The 2ND Joint NASA/FAA/DoD Conference on Aging Aircraft, Aug 31- Sep 3, 1998, Williamsburg, VA. NAS*A/C*P-1999-208982

[3] Fawaz, S. A., J. Schijve, and A. U. de Koning. "Fatigue Crack Growth in Riveted Lap-Splice Joints", Proc. of the 19th Symposium of the International Committee on Aeronautical Fatigue, 16-20 June 1997, Edinburgh, Scot. Scotland, UK: EMAS/SoMat Systems International Ltd, 1997

[4] Smith, F. W. and T. E. Kullgren, "Theoretical and Experimental Analysis of Surface Cracks Emanating from Fastener Holes," AFFDL-TR-76-104, Air Force Flight Dynamics Laboratory, Feb. 1977.

[5] Hechmer, J. L. and J. M. Bloom, "Determination of Stress Intensity Factors for the Corner-Cracked Hole Using the Isoparametric Singularity Element, International Journal of Fracture, Oct. 1977.

[6] Raju, I. S. and J. C. Newman, Jr., "Stress Intensity Factors for Two Symmetric Corner Cracks," Fracture Mechanics, ASTM STP 677, American Society for Testing and Materials, Ed. C. W. Smith, 1979, pp. 411-430.

[7] Bakuckas, John, G. Jr., "Comparison of Boundary Correction Factor Solutions for Two Symmetric Cracks in a Straight-Shank Hole." DOT/FAA/AR-98/36, 1999.

[8] Bartelds, G. and A. U. de Koning, "Application of Finite Element Methods to the Analysis of Cracks, (Phase I - Evaluation of Methods)," National Aerospace Laboratory of The Netherlands, NLR TR 78138 U, Dec. 1987.

[9] Fawaz, Scott Anthony. Fatigue Crack Growth in Riveted Joints. Diss. Delft University of Technology, 1997. Delft, NL.

[10] "STRIPE: For Self-Adaptive FE-Analysis of Three-Dimensional Structures, User's Manual Version 1 Preliminary," Structures Department, Aeronautical Research Institute of Sweden, 1988-11-01.

[11] Andersson, B., U. Falk, and I. Babuska. "Accurate and Reliable Determination of Edge and Vertex Stress Intensity Factors in Three-Dimensional Elastomechanics." Proceedings of the 17th Congress of the International Council of Aeronautical Sciences (ICAS), Stockholm, Sweden (1990): pp. 1730-1746

[12] von Petersdorff, T. "Randwertprobleme der Elastizitätstheorie für Polyedersingularitäten und Approximation mit Randelementmethoden." Ph.D. Thesis, Technical University of Darmstadt, Germany, 1989.

[13] Andersson, B, U. Falk, I Babuška, and T. von Petersdorff. "Reliable Stress and Fracture Mechanics Analysis of Complex Components Using a *h-p* version of FEM." International Journal of Numerical Methods in Engineering, 38 (1995): pp. 2135-2163.

[14] Babuska, I. and B. Andersson. "A Splitting Method for Fracture Mechanics Analysis." FFA-TN-1996-27, The Aeronautical Research Institute of Sweden, Stockholm 1996.

[15] Andersson, B., I. Babuska, and P. Stehlin. "Reliable 3D Multiple-Site Fracture Mechanics Analysis." FFA-TN-1998-18, The Aeronautical Research Institute of Sweden, Stockholm 1998.

[16] Andersson, B. "Reliable Analysis 3D Multiple-Site Fatigue Crack Growth." FFA-TN-1999-20, The Aeronautical Research Institute of Sweden, Stockholm 1999.

[17] Nilsson, Karl-Fredrik and Börje Andersson. "Analysis Methodology for Fatigue Crack Propagation and Residual Strength of Joints with Widespread Fatigue Damage." Proceedings of the 1999 Aircraft Structural Integrity Program Conference, San Antonio, TX 30 November – 2 December 1999.

[18] Gordon, W. J. and C. A. Hall. "Transfinite Element Methods: Blending-Function Interpolation over Arbitrary curved Element Domains." Numerische Matematik, 21(1973): pp. 109-129.

[19] Broek, D. Elementary Engineering Fracture Mechanics. Martinus Nijhoff Publishers, Dordrecht, 1986.

[20] Shah, R. C., "Stress Intensity Factors for Through and Part Through Cracks Originating at Fastener Holes," Mechanics of Crack Growth, ASTM STP 590, American Society for Testing and Materials, 1976, pp. 429-459.

[21] NASGRO Fatigue Crack Growth Computer Program, Version 2.01, NASA JSC-22267A, 1994.

[22] Harter, James A., "AFGROW Users Guide and Technical Manual," AFRL-VA-WP-TR-1999-3016, February 1999.

[23] Newman, Jr., J. C. and I. S. Raju. Stress Intensity Factor Equations for Cracks in Three-Dimensional Finite Bodies Subjected to Tension and Bending Loads. NASA-TP-85793, 1984.

[24] Newman, Jr., J. C. and I. S. Raju. "Prediction of Fatigue Crack-Growth Patterns and Lives in Three-Dimensional Crack Bodies." Advances in Fracture Research (Fracture 84), Sixth International Conference on Fracture, Vol 3, 1984, pp.1597-1608.

[25] Shah, R. C., "Stress Intensity Factors for Through and Part Through Cracks Originating at Fastener Holes," Mechanics of Crack Growth, ASTM STP 590, American Society for Testing and Materials, 1976, pp. 429-459.

[26] Atluri, S. N. and Pin Tong. "Computational Schemes for Integrity Analyses of Fuselage Panels in Aging Airplanes." Eds. S. N. Atluri, S. G. Sampath, and P. Tong. Structural Integrity of Aging Airplanes, Springer Series in Computational Mechanics. Berlin: Springer Verlag, 1991.

[27] Blom, A. F. and B. Andersson. "On the Semi-Elliptical Surface Crack Problem: Detailed Numerical Solutions for Complete Elastic Stress Fields." Surface-Crack Growth: Models, Experiments, and Structures, ASTM STP 1060, W. G. Reuter, J. H. Underwood, and J. C. Newman, Jr., Eds., American Society for Testing and Materials, Philadelphia 1990, pp. 77-98.

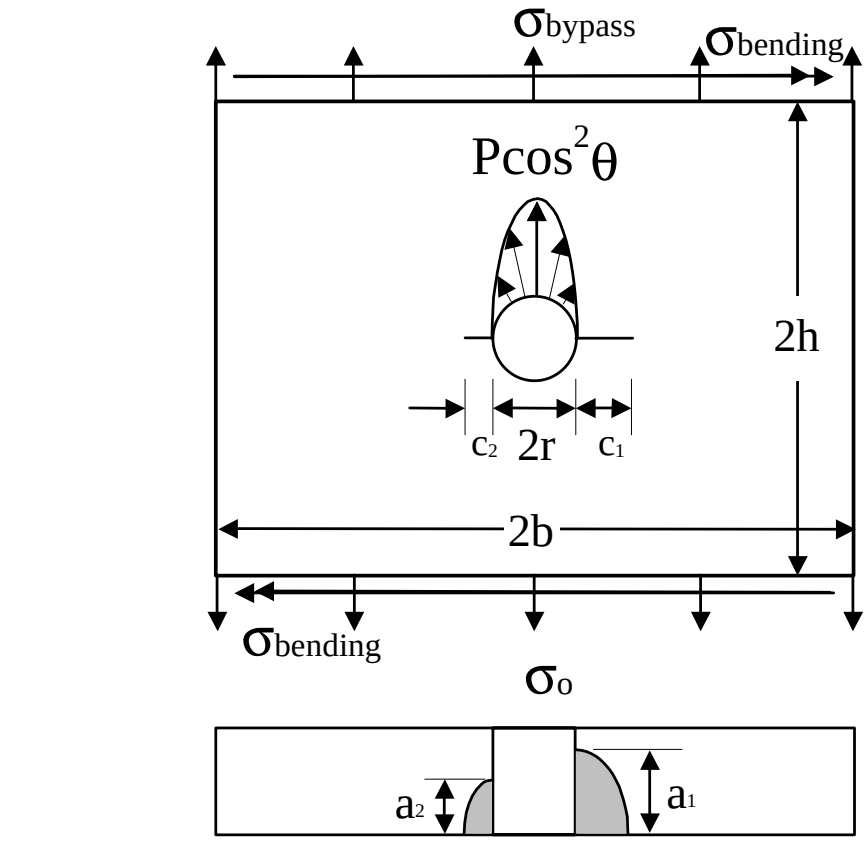

Figure 1 Parameter definition for two unequal corner cracks at centrally located hole in a finite width sheet subject to general loading

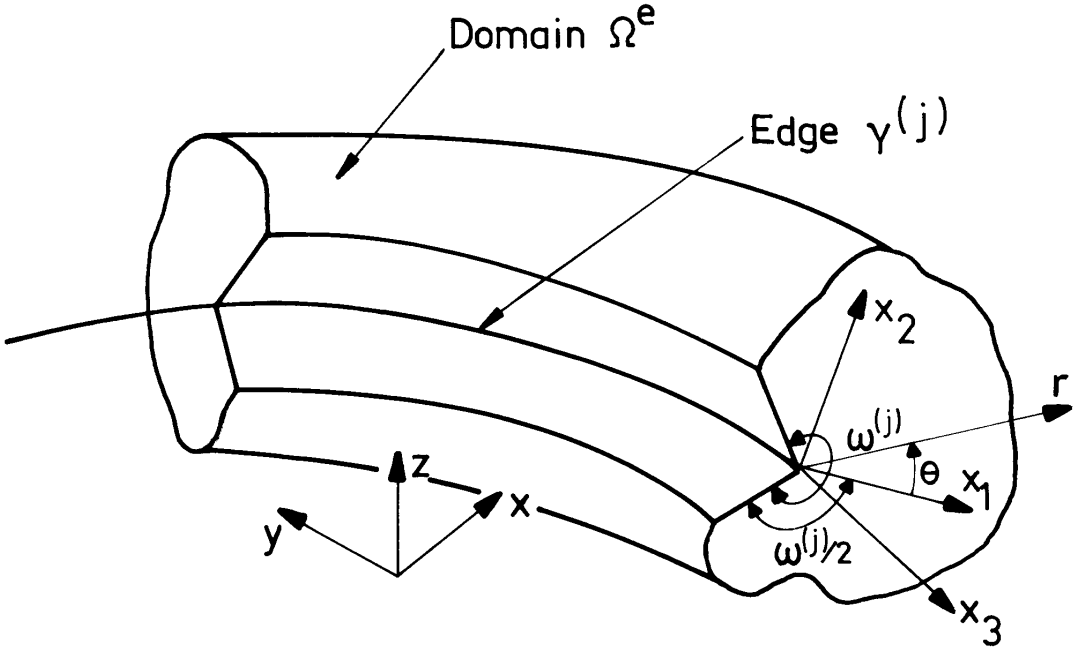

Figure 2 Local domain

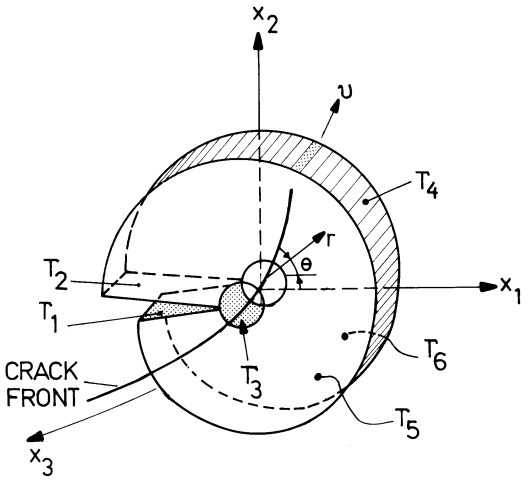

Figure 3 Domain Ω^e used for extraction of edge intensity functions

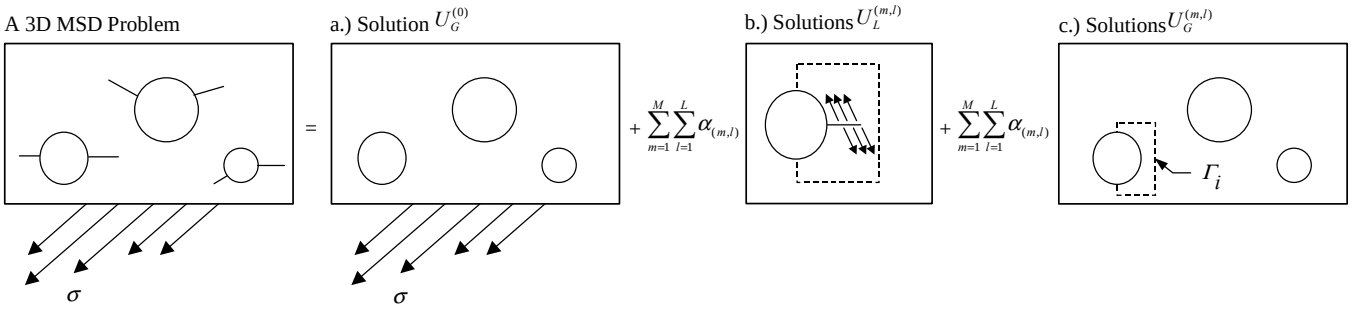

Figure 4 Splitting scheme sub-problems

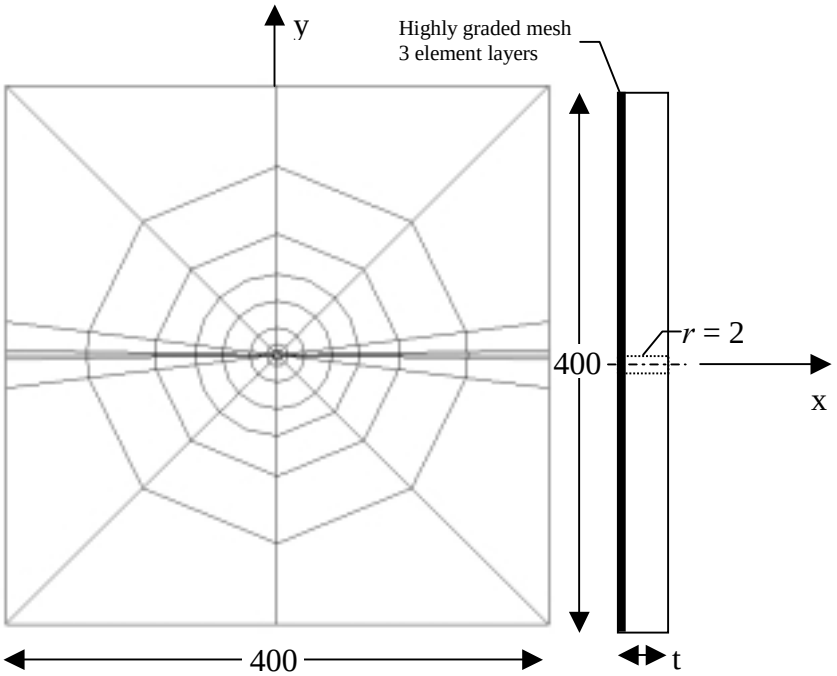

Figure 5 Global model used for all crack configurations and applied loads

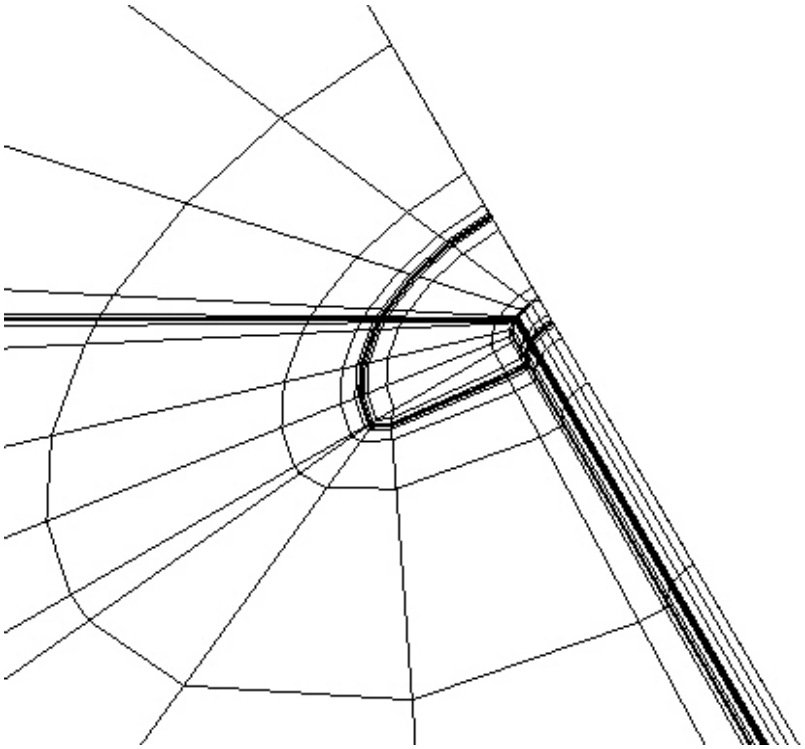

Figure 6 Par of local mesh: *a/c* = 0.8, *a/t* = 0.2. Note that only the polyhedral shape is depicted. In the FE-analysis, the hole surface has an exact cylindrical shape and the crack front has an exact elliptical shape.

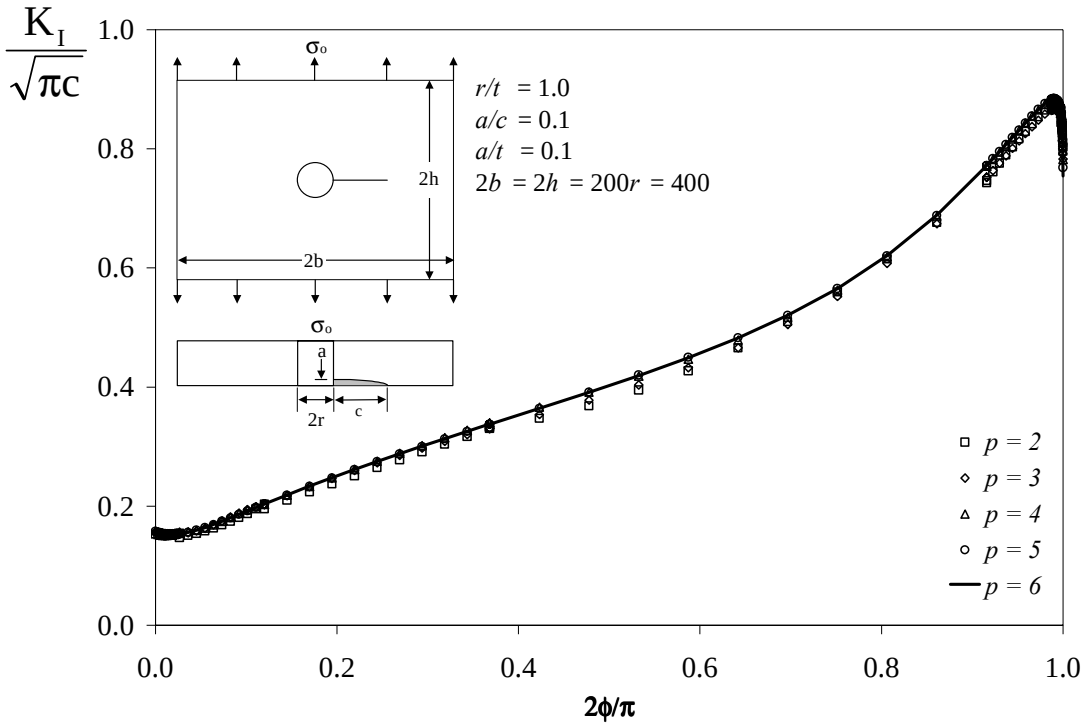

Figure 7 Convergence study for a single shallow corner crack at a hole subject to remote tension

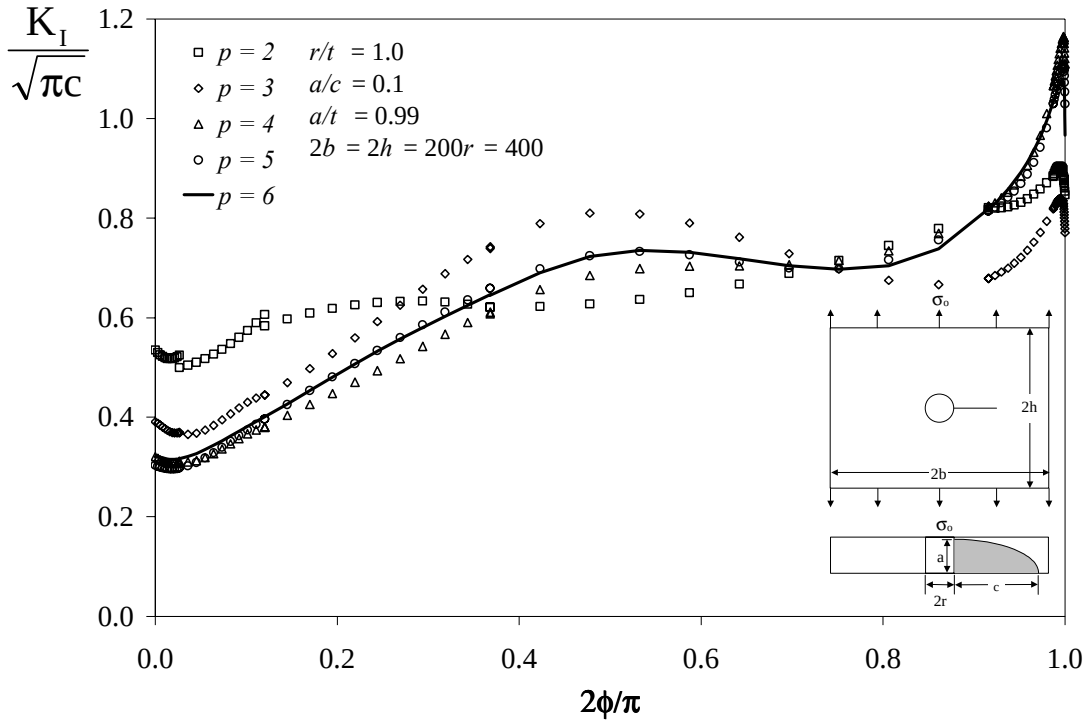

Figure 8 Convergence study for a single deep corner crack at a hole subject to remote tension

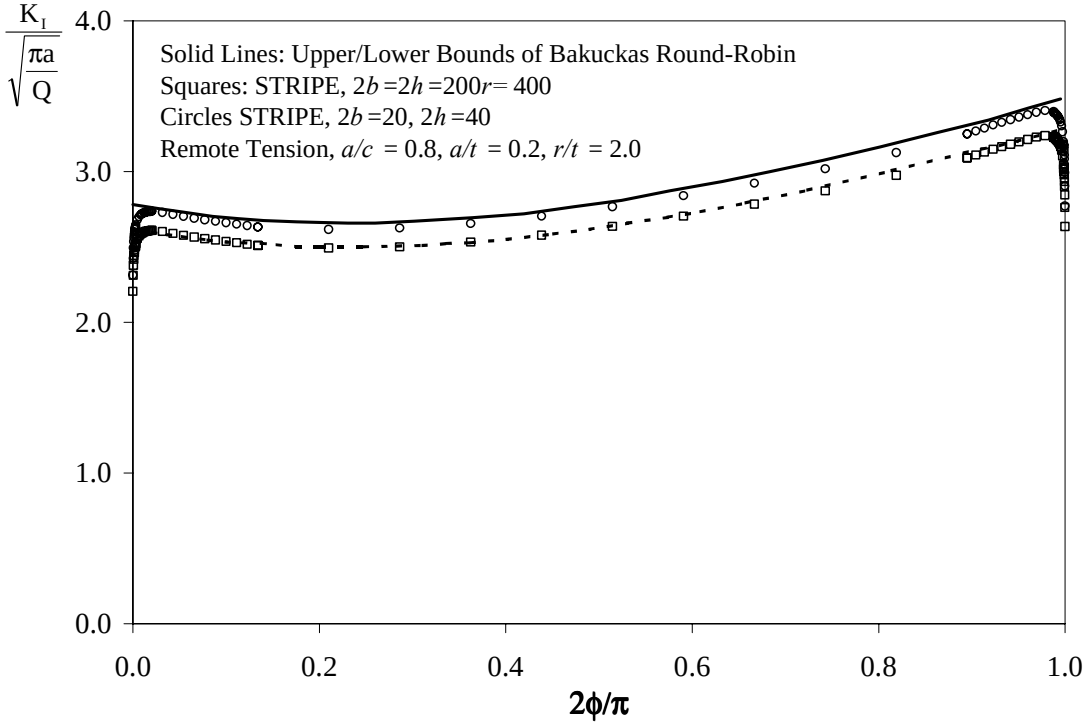

Figure 9 Comparison of published results[7] vs. STRIPE

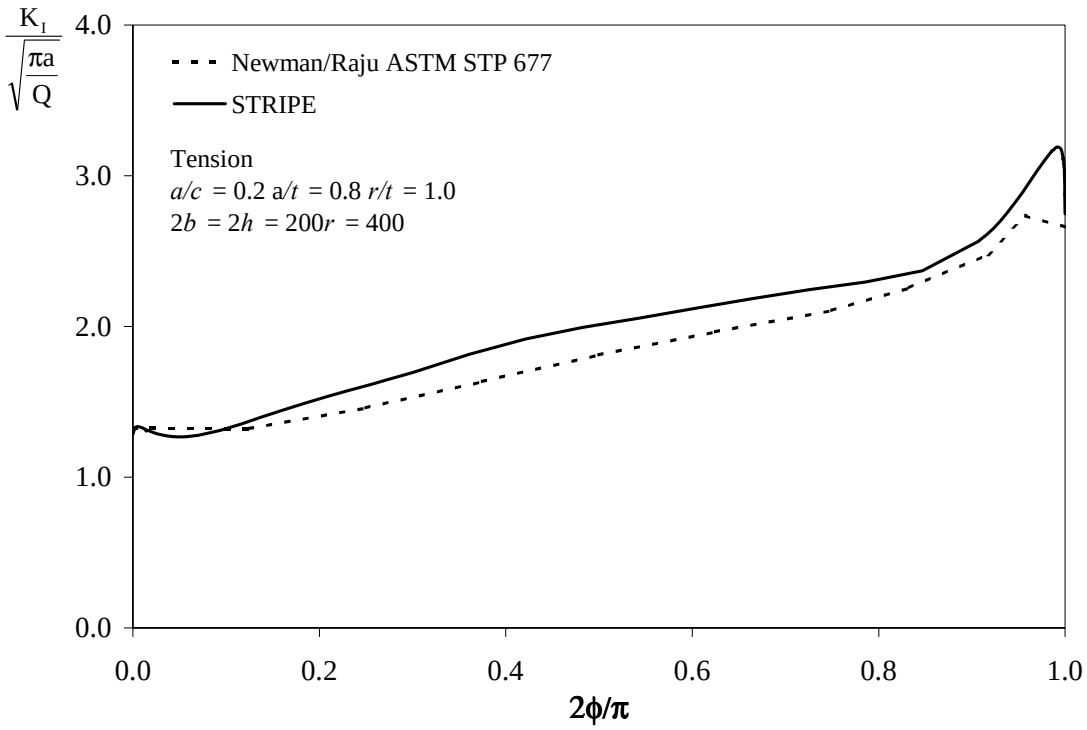

Figure 10A Tension K solution comparison for a deep crack

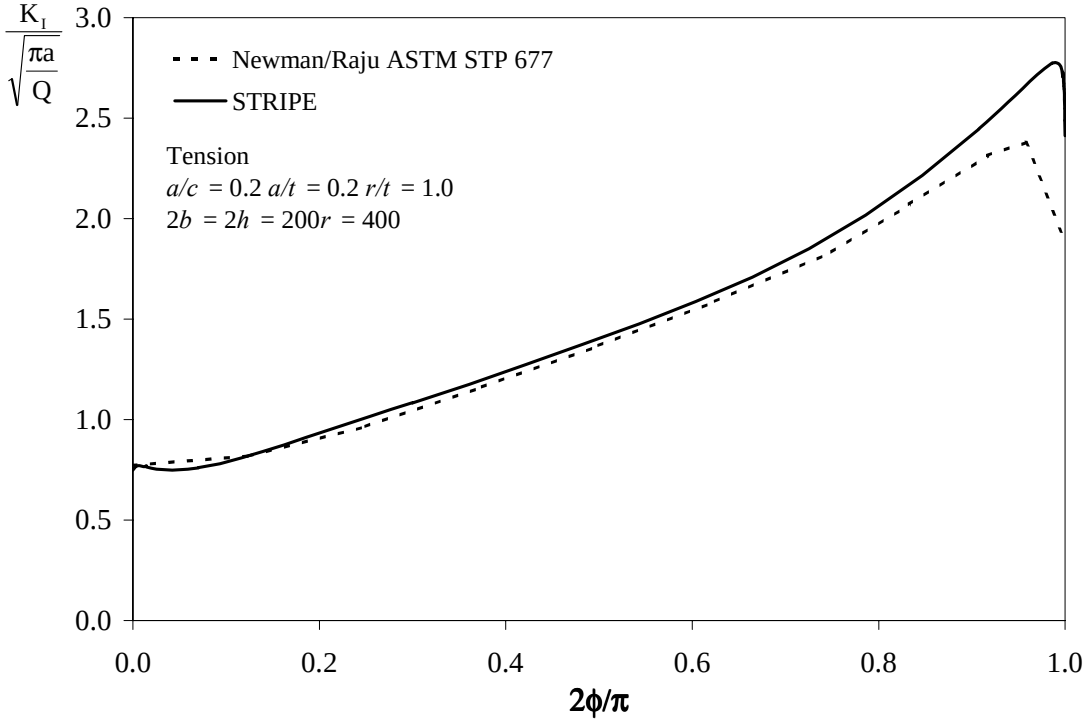

Figure 10B Tension K solution comparison for a shallow crack

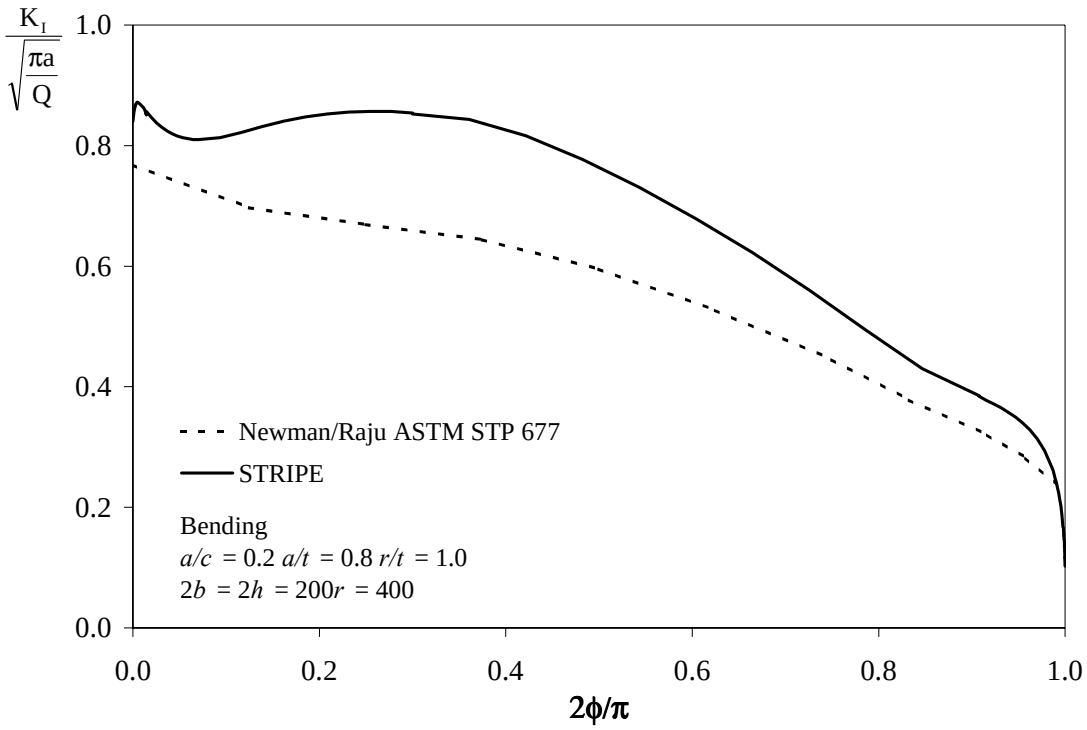

Figure 11A Bending K solution comparison for a deep crack

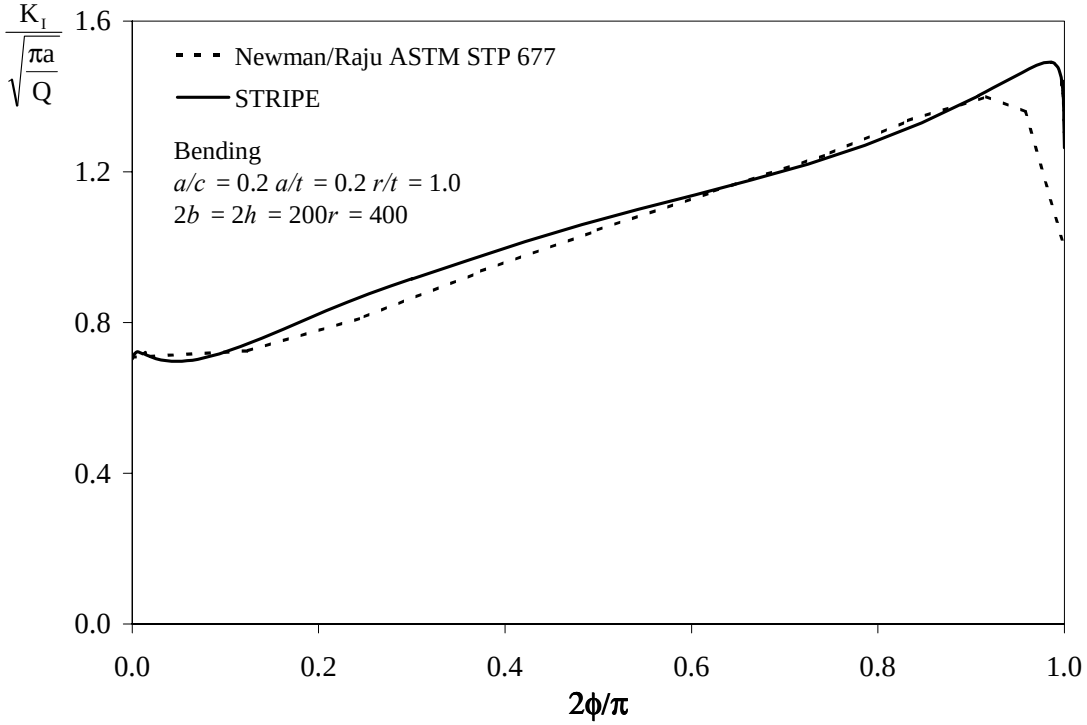

Figure 11B Bending K solution comparison for a shallow crack

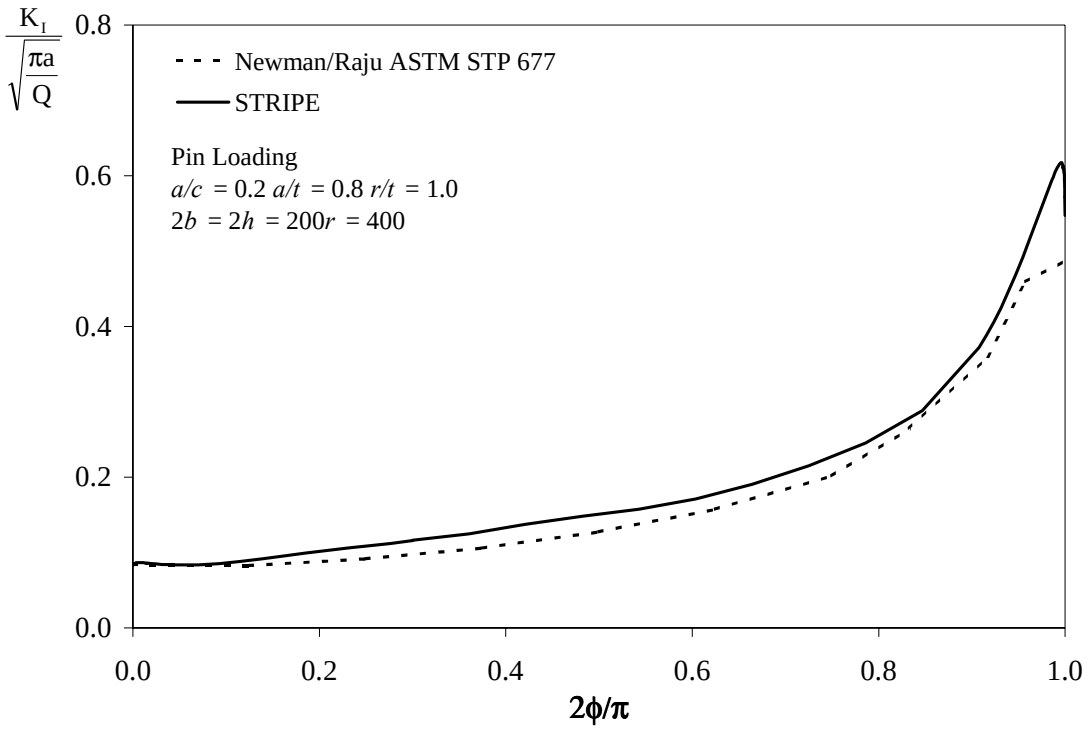

Figure 12A Pin Loading K solution comparison for a deep crack

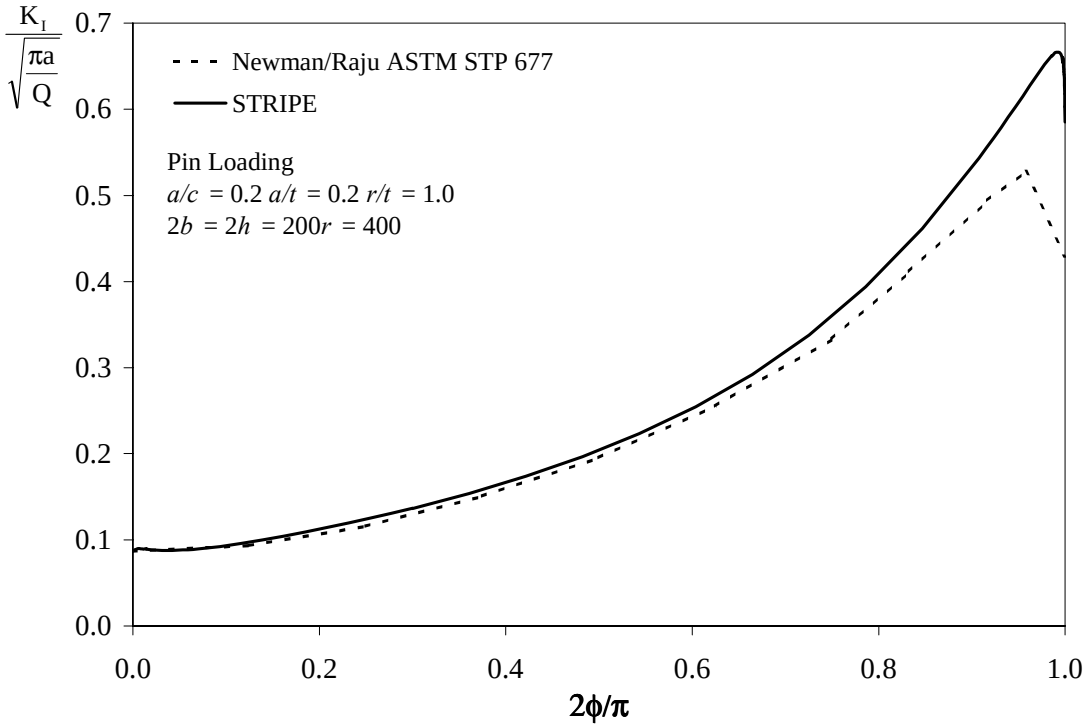

Figure 12B Pin Loading K solution comparison for a shallow crack

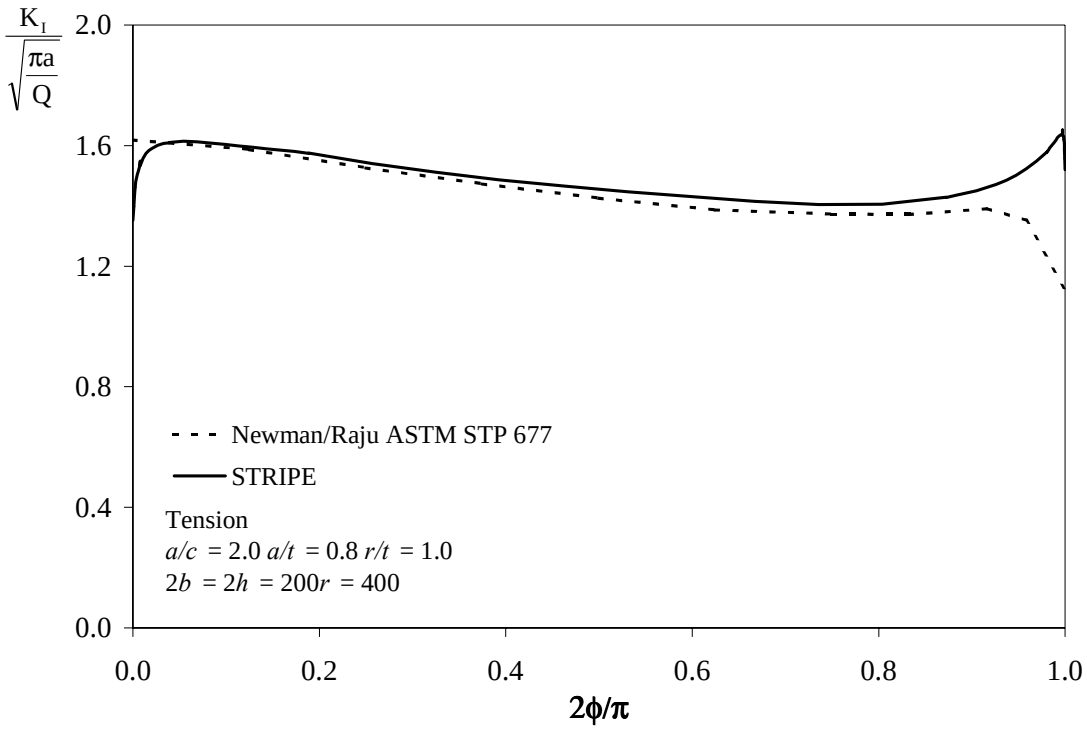

Figure 13A Vertex behavior for large, deep cracks in Tension

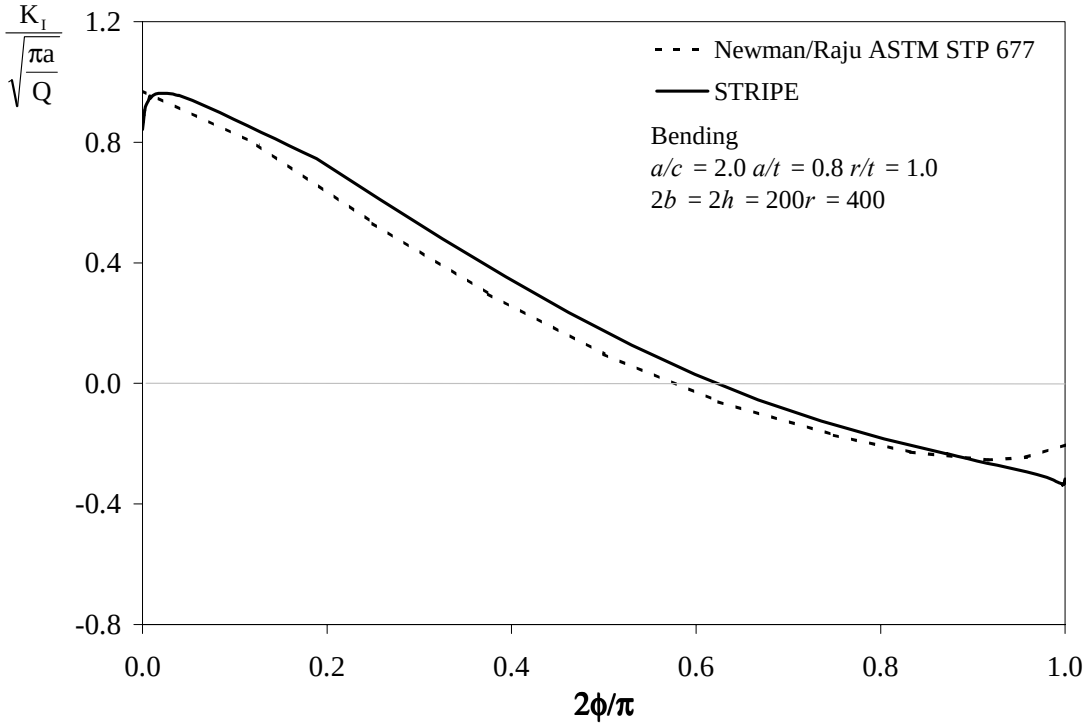

Figure 13B Vertex behavior for large, deep cracks in Bending

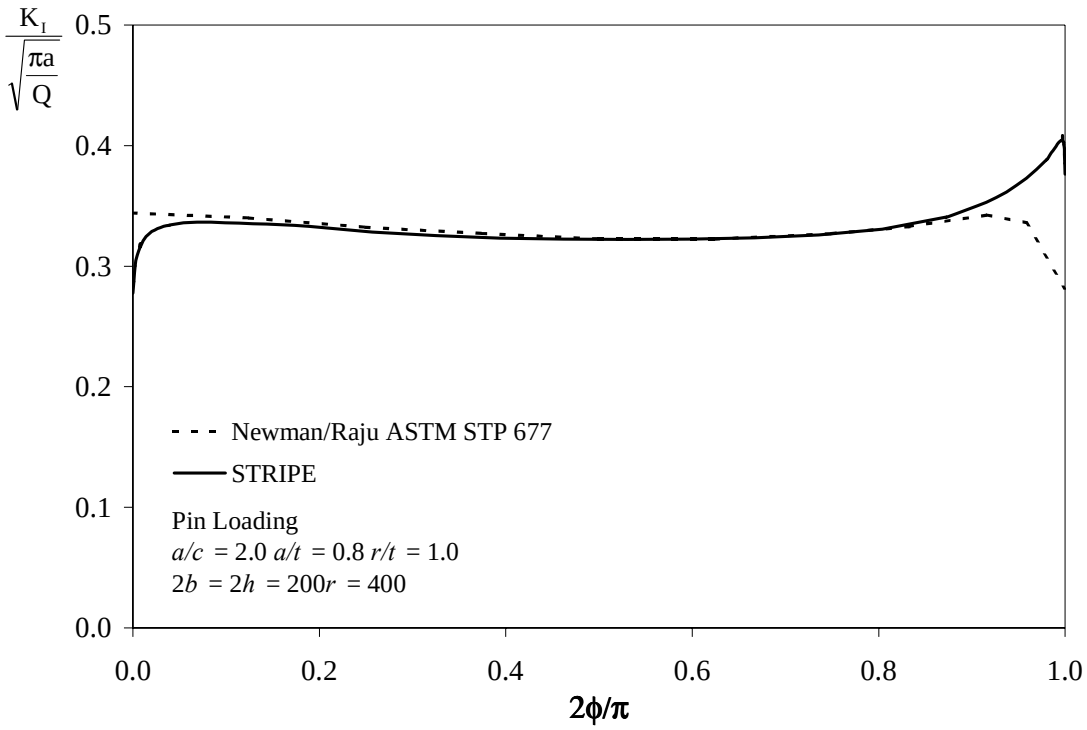

Figure 13C Vertex behavior for large, deep cracks in Pin Loading

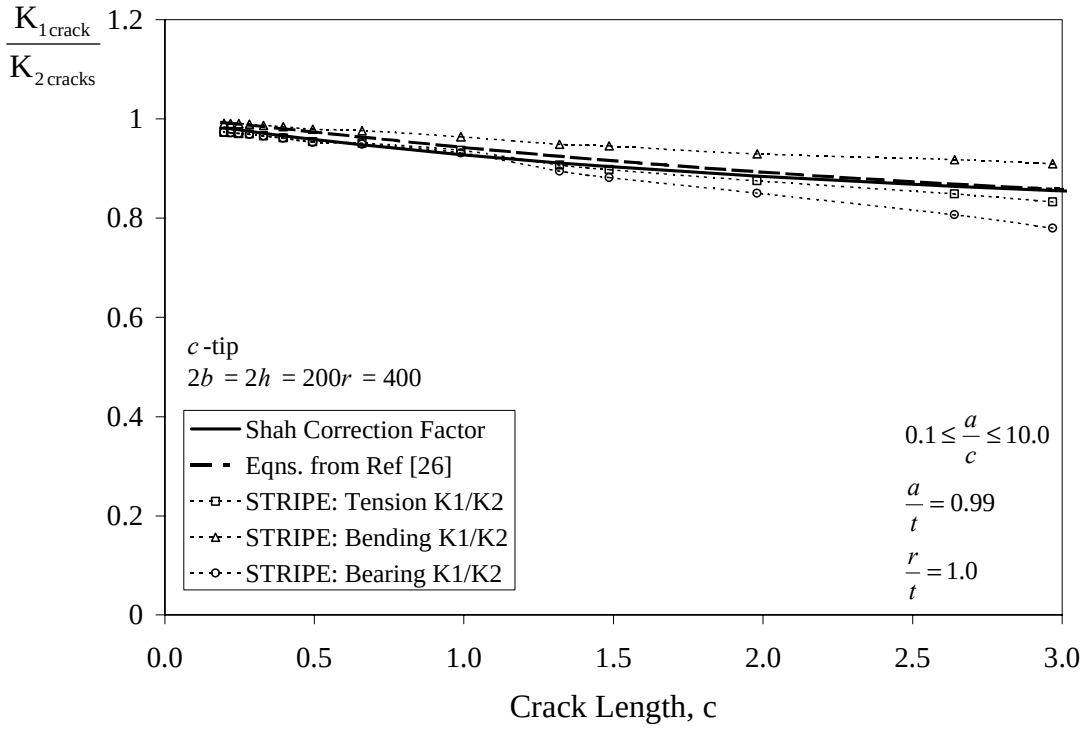

Figure 14A Comparison of conversion factors for 1 to 2 cracks at hole, *c*-tip

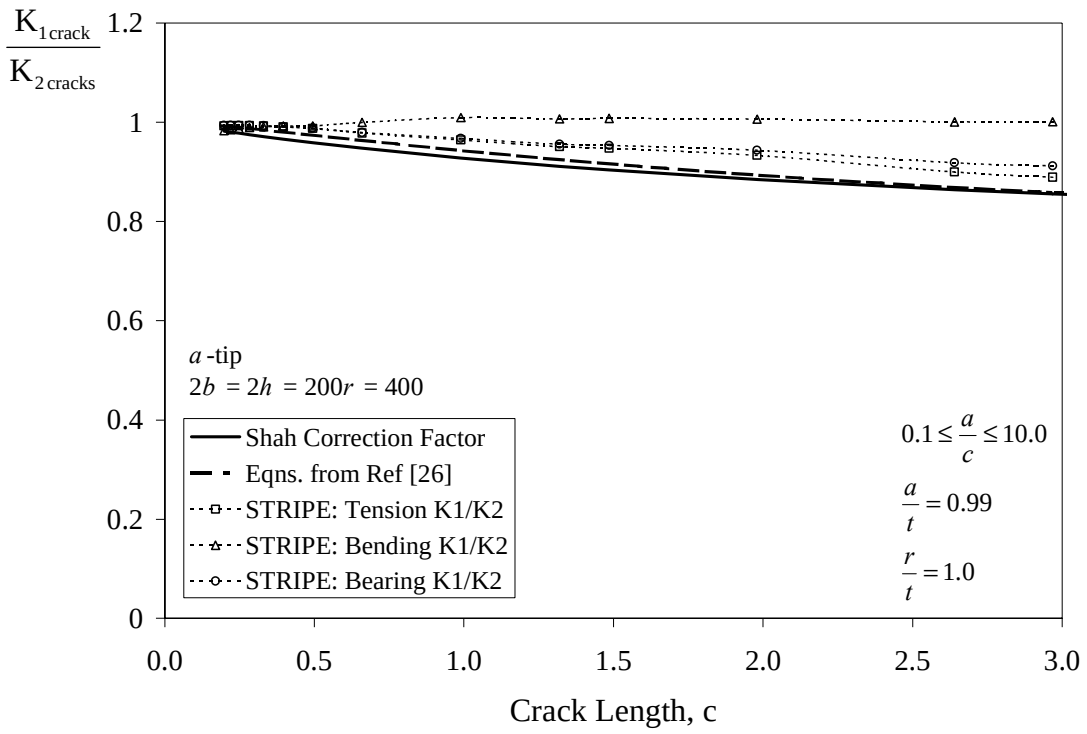

Figure 14B Comparison of conversion factors for 1 to 2 cracks at hole, *a*-tip

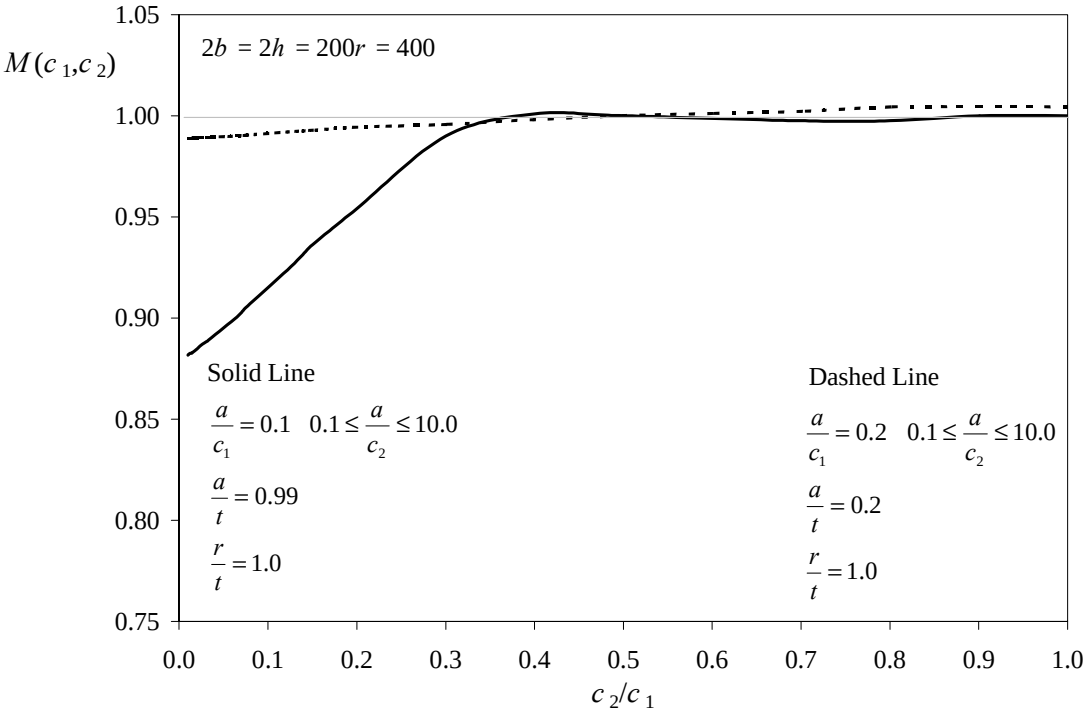

Figure 15 Effect of crack 2 on the K solution of crack 1

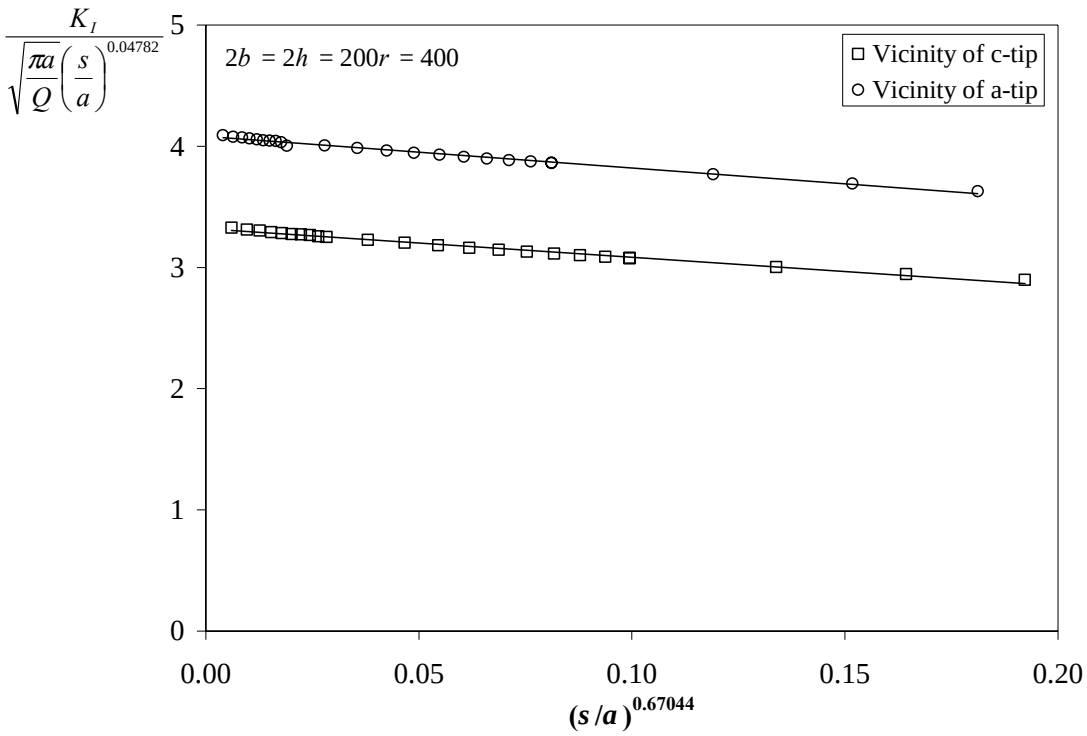

Figure 16 Characteristic K behavior near vertices for Bakuckas comparison